Materials Science-Poland, 35(1), 2017, pp. 159-172
http://www.materialsscience.pwr.wroc.pl/
DOI: 10.1515/msp-2017-0014

DE GRUYTER OPEN

Formation of Fe and Ni substituted $LiMn_{2-x}M_xO_4$ nanopowders and their crystal and electronic structure and magnetic properties

E. TALIK[1,*], L. LIPIŃSKA[2], A. GUZIK[1], P. ZAJDEL[1], M. MICHALSKA[2], M. SZUBKA[1], M. KĄDZIOŁKA-GAWEŁ[1], R.L. PAUL[3]

[1]Institute of Physics, University of Silesia, Uniwersytecka 4, 40-007 Katowice, Poland
[2]Institute of Electronic Materials Technology, Wólczyńska 133, 01-919 Warszawa, Poland
[3]Analytical Chemistry Division, National Institute of Standards and Technology, Gaithersburg, MD 20899, USA

The Pechini sol-gel method was applied to obtain $LiMn_{2-x}T_xO_4$ (T = Ni, Fe; x = 0.1 to 0.5) nanopowders. Crystal and electronic structures, chemical composition and magnetic properties of the materials were characterized by X-ray diffraction, XPS, SEM/EDX microscopy, prompt gamma-ray activation analysis (PGAA), Mössbauer spectroscopy and magnetic susceptibility, respectively. XRD measurements showed that the $LiMn_{2-x}Ni_xO_4$ were single phase for x = 0.1 and 0.2. Three samples with higher Ni content contained some addition of a second phase. Analysis of the oxidation state of the dopants by XPS revealed ionic Ni^{2+} and Fe^{3+}. Mössbauer spectroscopy also confirmed 3+ oxidation state of iron and its location in octahedral sites, which excluded the inverse spinel configuration. XPS examinations showed that Mn^{3+} ions dominated in the iron substituted series whereas the Mn^{4+} was dominant in the nickel series.

Keywords: *nanomaterials; lithium manganese nickel oxides; spinel*

1. Introduction

Lithium manganese oxide ($LiMn_2O_4$) spinel has been extensively studied as a cathode material for Li-ion batteries, as an alternative to $LiCoO_2$, $LiNiO_2$ or $LiFePO_4$ used today. Initially, $LiMn_2O_4$ spinel has been synthesized mainly using conventional solid state methods [1, 2]. Nowadays, other synthetic routes are applied too. One of them is a modified sol-gel (Pechini) technique, which seems to be appropriate for preparation of nanocrystalline cathode materials. Being a solution-based route, it offers a possibility of molecular level mixing of the starting materials. As a consequence, one can attain a high degree of homogeneity with small particle size and high surface area [3–6].

Application of $LiMn_2O_4$ offers several advantages, like low cost, easy preparation, non-toxicity, high potential (∼4 V vs. lithium metal), satisfactory capacity, high energy density, low self-discharge and high thermal stability [7–10].

In spite of these advantages, $LiMn_2O_4$ suffers from a serious capacity fading during charge-discharge cycles, which is unacceptable for commercial applications. This problem can be caused by several factors: manganese dissolution, electrolyte decomposition at high potentials, the Jahn-Teller (J-T) distortion at the state of a deep discharge and lattice instability [11, 12]. The last factor seems to be crucial for high cycling capacity of lithium manganese oxide [13]. There are various strategies to improve the structural stability of $LiMn_2O_4$. One of them is a partial substitution of manganese ions by other divalent or trivalent metal elements in the 16d octahedral sites in the spinel structure [1] in order to block the propagation of the J-T distortion. The doping elements are metals: either non-transition, e.g. Al, Mg [14–19], or transition metals Ni [20–31], Fe [14, 32–41].

*E-mail: talik@us.edu.pl

The substitution range is indeed wide: from 0.5 % up to 25 % of atomic fraction.

In our previous work [42], we synthesized lithium manganese oxide spinels with Mn substituted by transition metals (Fe and Ni) and non-transition metals (Mg and Al). The degree of B spinel site substitution was 25 % for all metal atoms (M), based on general formula of the substituted spinel $LiMn_{2-x}M_xO_4$, where x = 0.5. The samples were characterized by the following methods: X-ray diffraction (XRD), scanning electron microscopy (SEM/EDX), X-ray photoelectron spectroscopy (XPS) and SQUID magnetometry. XPS was used to examine the chemical composition and oxidation state of the manganese, in particular the Mn^{3+}:Mn^{4+} ratio, from the deconvolution of the complex Mn3p lines. The size of the grains and crystallites were independently obtained from SEM images and XRD patterns, respectively.

In this work, we continue examination of $LiMn_2O_4$ substituted by transition metals Fe and Ni, expanding the substitution range from 0.1 up to 0.5. We studied how the degree of substitution affects the structural and magnetic properties of lithium manganese spinels.

2. Experimental

The spinel structured lithium manganese oxide nanomaterials: $LiMn_{2-x}M_xO_4$, where M = Ni, Fe and $0.1 \leqslant x \leqslant 0.5$ (corresponding to nominal Mn:Fe or Mn:Ni composition ratios of 1.9:0.1, 1.8:0.2, 1.7:0.3, 1.6:0.4 and 1.5:0.5, respectively) were synthesized by a simple, low cost, modified sol-gel method [5, 6, 42–45].

First, stoichiometric amounts of metal precursors: manganese acetate $(C_4H_6O_4)Mn{\cdot}4H_2O$, (pure p.a. 99 % CHEMPUR) lithium acetate $(C_2H_3O_2)Li{\cdot}2H_2O$ ($\geqslant$ 97 %, Sigma-Aldrich) and nickel acetate $(C_4H_6O_4)Ni{\cdot}4H_2O$ (98 %, Sigma-Aldrich) or iron citrate $(C_6H_5FeO_7{\cdot}H_2O)$ (pure p.a., 18 % to 20 % Fe basis, Sigma-Aldrich) were separately dissolved in deionized water under continuous stirring. In the second step, the solutions were mixed together and stirred. The molar ratio of total metal ions and citric acid was 1:1. For example to obtain $LiMn_{1.9}Ni_{0.1}O_4$, 1.9 mole of manganese acetate tetrahydrate 0.1 mole of nickel acetate tetrahydrate and 1 mole of lithium acetate dehydrate were used.

Next, for the Ni doped series, citric ($C_6H_8O_7{\cdot}H_2O$, pure p.a., 99.5 %, Avantor Performance Materials Poland S.A.) and acetic ($C_2H_4O_2$, 99.5 % CHEMPUR) acids were added as complexing agents. Finally, the solution was evaporated until a gel was formed, which was further dried for a few hours at 150 °C. The prepared xerogels were ground in an agate mortar to obtain fine powders. The powders were heated in air flow from room temperature to 300 °C with the heating rate of 10 °C/min and maintained at this temperature for 3 hours. Then, the samples were heated at the same rate to 700 °C and maintained at this temperature for next 5 hours. After completion of the calcination stage the nanocrystalline powders were cooled down freely.

For the iron doped series, the chelating agent: citric acid monohydrate ($C_6H_8O_7{\cdot}H_2O$) with ethylene glycol (99 % CHEMPUR) were added to the solution. The solutions were dried for several hours at 150 °C. The obtained powders were ground in an agate mortar and heated for several hours in air in the temperature range of 300 °C up to 700 °C.

Powder diffraction studies were carried out on a PANalytical PW1050 diffractometer in Bragg-Brentano geometry. A nickel filtered $CuK\alpha_{1,2}$ source operating at 30 kV/30 mA was used to collect patterns with step size 0.02° and within angular range from 10° to 135°. The Rietveld method [46] was applied to refine collected patterns using the Fullprof software [47].

Example patterns are shown in Fig. 1. The instrumental resolution file was obtained from the internal silicon standard (a = 5.4306 Å). As the width of the diffraction peaks was larger than the machine broadening, size and strain models appropriate for Laue class m3m (size = 15, strain = 14) were used with the Thompson-Cox-Hastings profile [48]. The anisotropic strain broadening was introduced in the quartic form [49]. The anisotropic Lorentzian size broadening was modelled using the spherical harmonic approach proposed by Jarvinen [50].

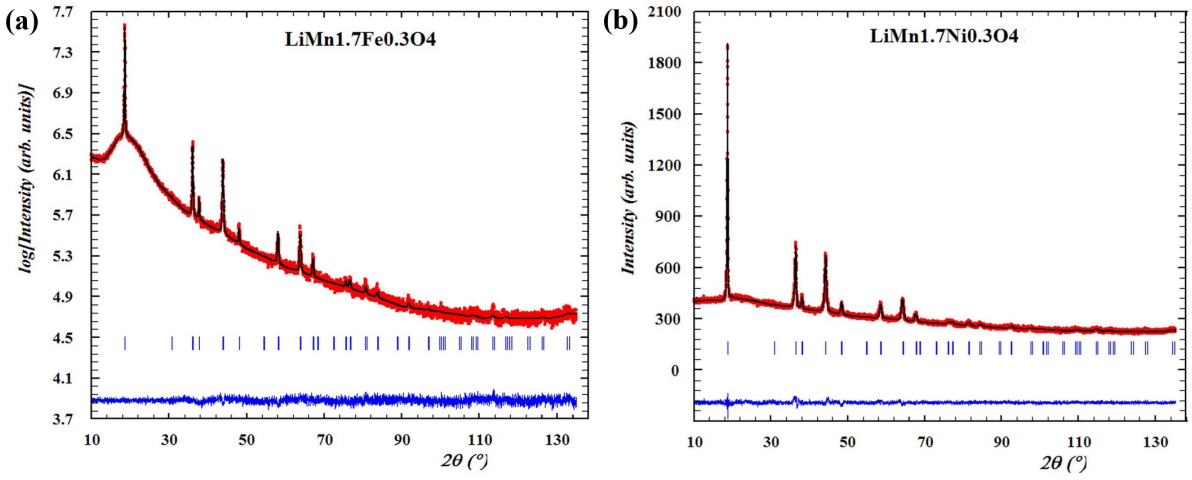

Fig. 1. Example XRD patterns for $LiMn_{1.7}Ni_{0.3}O_4$ and $LiMn_{1.7}Fe_{0.3}O_4$.

For all refinements, ionic form factors Li^+, Mn^{4+}, Mn^{3+}, Ni^{2+}, Fe^{3+} and O^{2-} were used. The presence of nickel in the 2+ rather than 3+ state in spinel oxides has been previously justified on the basis of higher stability in both $LiMn_2O_4$ [30, 51, 52] and prototypical $MgAl_2O_4$ [53] doped with Ni. Moreover, a similar conclusion has been drawn for selenide spinel $ZnCr_{2-x}Ni_xSe_4$ series [54] using X-ray absorption spectroscopy at the Ni K edge. Soft X-ray Absorption Spectroscopy (XAS) studies of a similar compound $LiMn_{0.5}Ni_{0.5}O_4$ [55] also found signatures of Ni^{2+} on the octahedral site. Due to the a priori unknown Mn^{4+}:Mn^{3+} ratio, two test refinements were performed in order to estimate its influence on the structural parameters. The first refinement was done only with the Mn^{3+} and the second one with Mn^{4+} ionic form factors. The obtained structural parameters were equal within one standard uncertainty, therefore only Mn^{3+} was used in all further refinements.

Parameters used in Rietveld refinement included: lattice parameters, displacement and transparency corrections, up to two size (K_{00}, K_{41}) and strain coefficients (S_{400}, S_{220}), one asymmetry parameter, 3 individual isotropic atomic displacement parameters (ADPs), where ADPs of atoms on the same crystallographic site were constrained to be equal. The background was treated as a linear interpolation between selected points. The refined size parameter K_{00} (Y_{00} spherical harmonic) described isotropic domain size [50] and K_{41} a fourth order deformation. The strain parameter S_{400} was used to quantify correlations along the main principal directions [49] and S_{220} between each of these directions. In two of the samples: $LiMn_{1.5}Ni_{0.5}O_4$ and $LiMn_{1.9}Ni_{0.1}O_4$, refinement of the higher terms of shape and strain was unstable, therefore only the K_{00} and S_{400} parameters were used. An attempt to refine site occupation factors of lithium and manganese vs. the dopant was also unsuccessful as lithium is very weakly seen by XRD and there is only small contrast between Mn and Fe/Ni. Wherever available, statistical uncertainties at 1σ level are reported in parentheses.

The microstructural observations of the nanopowders as well as the microcompositional analyses were conducted using the JOEL JSM-7600F Scanning Electron Microscope.

The XPS spectra were obtained using a PHI 5700/660 Physical Electronics Photoelectron Spectrometer with monochromatized AlKα X-ray radiation (1486.6 eV). A hemispherical mirror analyzer measured the energy of electrons with an energy resolution of about 0.3 eV. The photoelectron emission from a surface area of 800 μm × 2000 μm was recorded. All measurements were performed in the conditions of 10^{-8} Pa. In every case, a charge neutralizer was used because of the charge effect which

occurs for non-conducting samples. The binding energy was determined with reference to the C 1s component set at 285 eV. Each peak of the recorded spectrum is characteristic of a certain electron energy level of the measured elements. However, the measured binding energies are not absolutely constant but depend on the chemical environments, where functional groups are located due to modification of the valence electron distribution. These differences in electron binding energies in relation to pure element are called chemical shifts. The angle between the X-ray source and the sample surface was 45°.

For XPS investigations, it is important to determine the relative concentrations of various constituents. The Multipak Physical Electronics program [56] enables quantification of the XPS spectra utilizing peak area and sensitivity factor. The standard atomic concentration calculation provides a ratio of each component to the sum of all elements taken into account in the data. Identification of all elements, except H and He, is detectable within a limit of the order 0.1 at.% for good quality spectra. Only those elements are considered for which the specific line is clearly visible in the spectrum. For these lines, the background individually selected in the region limited to the particular line is subtracted and after that integration of the peak area is performed [56]. The Gaussian-Lorentzian functions were used to fit the XPS core level spectra.

Magnetic susceptibility was measured using the SQUID Magnetometer MPMS-XL-7AC (Quantum Design) in the temperature range of 2 K to 400 K.

The ^{57}Fe Mössbauer spectrum was recorded at room temperature using a constant acceleration spectrometer with ^{57}Co:Cr source. The spectrometer velocity was calibrated with a high purity α-Fe foil. The values of isomer shifts (IS) for all identified subspectra were determined relatively to the α-Fe standard.

Determination of Mn:Li and Mn:Ni ratios in Li, Mn, Ni oxides was performed by cold neutron prompt gamma-ray activation analysis (PGAA). The five analyzed samples were in the form of powders, weighing between 30 mg and 60 mg. All were derivatives of $LiMn_2O_4$, with a fraction of the Mn replaced by Ni. The samples were sealed in Teflon® Bags and analyzed using the NG7 cold neutron PGAA instrument located at the NIST Center for Neutron Research [57–59]. Irradiation times for samples ranged from 18 h to 24 h.

Standards for measurement of Mn:Li ratios were prepared from mixtures of Li_2CO_3 with (1) Mn_3O_4; (2) MnO_2, previously prepared for measurement of Li:Mn ratios in Li:Mn oxides. These were prepared by weighing components of the mixture in a mixing vial and shaking for 20 + 20 minutes using a SPEX Mixer/Mill. A 0.3 g to 1 g portion of each powdered mixture was pressed into a pellet, sealed in a Teflon® Bag, and irradiated for several hours in the prompt gamma beam. Additional standards for measurement of Mn:Ni ratios were prepared from a mixture of Ni powder, MnO_2, and graphite, mixed similarly. Two pellets, weighing 0.3 g and 0.6 g were prepared from the mixture as described above.

Calculations were performed using the ^{7}Li capture gamma ray at 2032 keV, Mn gamma rays at 5015 keV and 7244 keV, and the Ni capture line at 8998 keV. The peaks were integrated using the SUM4 algorithm [60]. Sensitivities ratios calculated for the mixtures of Li_2CO_3 with Mn compounds were used to determine mass content of Li and Mn. A mass ratio of Li:Mn was first obtained, which was then converted to moles Li/mol Mn. Molar ratios for Mn:Ni were similarly calculated using the ratios calculated from Ni:MnO_2/graphite standards.

3. Results and discussion

3.1. X-ray diffraction

It is well established that $LiMn_2O_4$ undergoes a charge ordering transition accompanied by an orthorhombic distortion due to the J-T cooperative effect, close to room temperature [61]. The observed $3 \times 3 \times 1$ superstructure is one of the factors limiting cycling performance of Li-ion batteries.

Substitution of manganese with nickel in spinel lithium manganates has been reported earlier in nanosized form for $x = 0.5$ [30, 42] as well as polycrystalline phases for $x = 0.05$, 0.07 and 0.5 [21,

51, 52] and it was sufficient to block the long range J-T transition in favor of the cubic spinel structure. At the same time, a study of the local environment using Raman spectroscopy [30] revealed line splitting characteristic of a lower symmetry space group ($P4_332$), which could indicate structural distortion due to cation ordering, similar to the one observed in Mg doped compounds [52]. However, in the latter paper the authors did not find any signature of long range cation ordering in the neutron diffraction pattern of the $LiMn_{1.5}Ni_{0.5}O_4$ [52].

The lack of long range cation ordering in nanosized $LiMn_{1.5}Ni_{0.5}O_4$ was also corroborated in our earlier paper [42]. In the current study, the observation was extended to the whole substitution range x = 0.1 to 0.5.

In all cases, lattice parameters of the Ni doped samples were shorter than for the undoped $LiMn_2O_4$, although they differed on absolute scale (Table 1). It must be noted that the lattice parameters of $LiMn_2O_4$ depend on conditions of synthesis, which was reported earlier [62].

The decrease of the lattice parameter with increased level of nickel doping in the octahedral cation site might be at first surprising as the ionic radius of Ni^{2+} (0.69 Å) is larger than the radii of Mn^{3+} 0.58 Å in low spin (LS) and 0.65 Å in high spin (HS) forms [63].

The increase of the lattice parameter by a larger size of Ni^{2+} is compensated by the simultaneous conversion of the Mn^{3+} into Mn^{4+} which is expected to maintain the charge neutrality. The ionic radius of Mn^{4+} is the smallest of all of the radii and equal to 0.53 Å. Roughly estimating, on average and assuming that Mn^{3+} is only in HS form, substitution of x = 0.5 of Ni^{2+} should eliminate Mn^{3+} and produce a net decrease of lattice parameter of (0.69 – 0.65) – (0.65 – 0.53) = – 0.08 Å. The observed shortening of the lattice from 8.22 Å to 8.17 Å, i.e. only 0.05 Å might be explained by possible lithium overstoichiometry which was reported earlier by Strobel et al. [64]. The location of Li^+ in the octahedral site would shift the charge balance for the undoped sample into the Mn^{4+} side, therefore the effect of doping would be lower. The large spread of lattice parameters caused by the nonstoichiometric lithium has already been shown [42] for $LiMn_2O_4$ synthesized by a sol-gel method, similar to the route used in this paper. However, as it has been already pointed out by Berg et al. [21], the decrease in lattice parameters might be also caused by stronger Ni–O bonding.

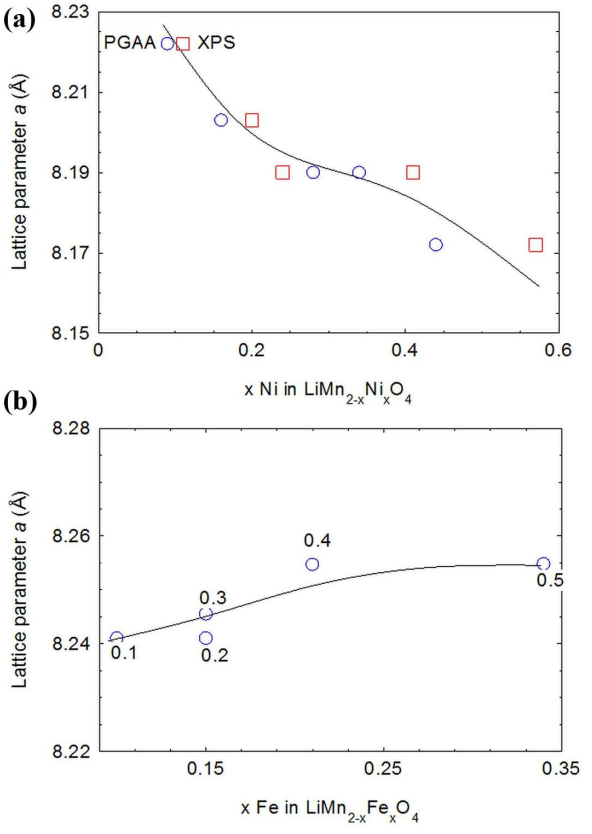

Fig. 2. Lattice parameter dependence (a) on nickel concentration for $LiMn_{2-x}Ni_xO_4$ (the real concentrations were obtained by XPS and PGAA methods); (b) on iron concentration for $LiMn_{2-x}Fe_xO_4$ (the real concentrations were obtained by XPS method).

The lattice parameters in the Ni doped series decreases monotonically up to x = 0.3 where a second phase starts to appear, which indicates that the solid solution is close to the solubility limit. The second phase with reflections at d = 2.40 Å, 2.07 Å and 1.47 Å is visible up to x = 0.5 and cannot be indexed by lowering of the symmetry of the spinel phase. The limit is also visible in the lattice parameter plot (Fig. 2a), where the dependence flattens

Table 1. Profile parameters obtained from the Rietveld refinement of the Ni doped series (CDS is Coherent Domain Size; estimated shape anisotropy is reported in curly brackets).

Nominal composition	a [Å]	V [Å^3]	CDS [nm]	Strain [%]	SG	Comment
$LiMn_{1.9}Ni_{0.1}O_4$	8.222(1)	555.9(2)	91{1}	0.25(5)	Fd3m	pure
$LiMn_{1.8}Ni_{0.2}O_4$	8.203(2)	552.0(2)	36{7}	0.25(2)	Fd3m	pure
$LiMn_{1.7}Ni_{0.3}O_4$	8.190(1)	549.4(2)	58{32}	0.40(6)	Fd3m	+2nd phase
$LiMn_{1.6}Ni_{0.4}O_4$	8.190(1)	549.3(2)	107{78}	0.52(5)	Fd3m	+2nd phase
$LiMn_{1.5}Ni_{0.5}O_4$	8.172(2)	545.8(2)	43{1}	0.12(2)	Fd3m	+2nd phase
$LiMn_{1.5}Ni_{0.5}O_4$	8.167(1)	544.7(2)	51{10}	0.0800(1)	Fd3m	[43]
$LiMn_2O_4$	8.207(1)	552.8(1)	80{7}	0.3101(1)	Fd3m	[43]
$Li_{1.12}Mn_{1.88}O_4$	8.2232(4)	556.1			Fd3m	[64]
Undoped	8.2228(4)				Fd3m	[52] NPD
Ni(II) 0.07	8.2156(1)				Fd3m	[52] NPD
$LiMn_{1.5}Ni_{0.5}O_4$	8.16594(3)					[53] XRD
$LiMn_{1.5}Ni_{0.5}O_4$	8.1690		36.9		Fd3m/P4$_3$32	[31] XRD

out for x = 0.3 and 0.4 proving that no more material is incorporated into the lattice. The last sample with Ni content x = 0.5 regains the trend but with a smaller slope which can be again explained by the appearance of the second phase. The restoration of the structural quality for x = 0.5 can be explained on the basis of the argument given already by Branford et al. [52]. The authors in question noted that the cation structural unit (Fig. 8 therein) was built of 4 cations which stabilized the configurations of 1:3 or 2:2 (1:1). In our case, the x = 0.5 sample is an example of 1:3 ratio (0.5 Ni:1.5 Mn).

The onset of phase separation is also reflected in the increasing lattice strains and growing size anisotropy (Table 6: rapid increase of the S_{220} coefficient and K_{41} parameter). In all cases, the sizes of the coherent scattering domains are under 100 nm. The refinement of the oxygen position was also performed, but the results reported in Table 6 and Table 7, because of its smaller reliability as oxygen atoms, are poorly seen by X-ray diffraction (Table 6) and depend on other elements in the unit cell. For the same reason, isotropic atomic displacement parameters (ADPs) are also reported in Table 6 and Table 7.

All samples in the iron doped series were obtained as single phase cubic materials with the spinel space group Fd3m. Lattice parameters were found to increase with an increasing Fe concentration (Table 2) and for the x = 0.5 sample were similar to those reported earlier in the literature, like sample L16A [42].

The lattice parameter increase with higher iron content (Fig. 2b) is only possible if Fe^{3+} substitutes Mn^{4+} or Mn^{3+} but in a low spin state (LS). It is evident if one notices the ionic radii series (all values in Å) Mn^{4+} (0.53) < Fe^{3+} (LS 0.55) < Mn^{3+} (LS 0.58) < Fe^{3+} HS (0.645) < Mn^{3+} (HS 0.65) [63].

Despite the monotonic changes in lattice and anion parameters, the samples with the highest iron content stand out from the rest. It is reflected in several of their properties:
(a) the lattice parameters deviate from the trend set out by x = 0.1 to 0.3 (Fig. 2b),
(b) the coherent domain size as well as the respective strain are twice as much (Table 2 and Table 7).

The above facts suggest that there is a qualitative difference between samples x = 0.1 to 0.3 and x = 0.4, 0.5, although the XRD analysis does not indicate any presence of a phase transition. It might be just a mere consequence of a preference to form better crystallized domains or an effect of iron clustering.

The oxygen position for the iron doped series (Table 7) was refined using nominal iron content and octahedral position, which was corroborated by

Table 2. Profile parameters obtained from the Rietveld refinement of the Fe doped series (CDS is Coherent Domain Size; estimated shape anisotropy is reported in curly brackets).

Nominal composition	a [Å]	V [Å^3]	CDS [nm]	Strain [%]	SG	Comment
$LiMn_{1.9}Fe_{0.1}O_4$	8.241(1)	559.7(1)	64{1}	0.15(3)	Fd3m	pure
$LiMn_{1.8}Fe_{0.2}O_4$	8.241(1)	559.7(1)	43{1}	0.14(2)	Fd3m	pure
$LiMn_{1.7}Fe_{0.3}O_4$	8.2454(8)	560.54(9)	50{1}	0.15(2)	Fd3m	pure
$LiMn_{1.6}Fe_{0.4}O_4$	8.2546(6)	562.46(7)	250{1}	0.22(4)	Fd3m	pure
$LiMn_{1.5}Fe_{0.5}O_4$	8.2547(6)	562.47(7)	113{1}	0.24(4)	Fd3m	pure
$LiMn_2O_4$	8.207(1)	552.8(1)	80{7}	0.3101(1)	Fd3m	[43]
$Li_{1.12}Mn_{1.88}O_4$	8.2232(4)	556.1			Fd3m	[64]
Undoped	8.2228(4)				Fd3m	[52] NPD
$LiMn_{1.5}Fe_{0.5}O_4$	8.258(1)	563.1(2)	51{3}	0.2444(1)	Fd3m	[43]

Mössbauer spectroscopy and is also reported in Table 6 and Table 7.

3.2. SEM imaging

SEM images show the morphologies of grains in the examined compounds at magnification of 50000× (Fig. 3). The obtained powders can be considered as nanocrystalline materials because a large number of the grains are close to 100 nm. The exceptions are the samples doped with Ni and Fe with x = 0.4.

3.3. PGAA

Ratios obtained using the data from each standard were averaged. Table 3 gives the final values of moles Mn/mol Li and moles Mn/mol Ni for each sample. Expanded uncertainties were determined by adding uncertainties from counting statistics, reproducibility of Mn (from the standard deviation of two values from each gamma-ray line/sqrt(2)), and the standard uncertainty: standard deviation of values obtained from the two standard pellets/sqrt(2), and multiplying by a coverage factor of 2. Mn:Ni ratios for all samples are in agreement with the values calculated from the nominal stoichiometry. Mn:Li ratios are lower than stoichiometric values for all samples, however this may be due in part to poor counting statistics for Li due to the low neutron capture cross section and small sample size.

3.4. Mössbauer spectroscopy

The fitting parameters of the Mössbauer spectrum of $LiMn_{1.5}Fe_{0.5}O_4$ (Fig. 4) are listed in Table 4. The data displayed give clear evidence that Fe^{3+} ions occupy two different octahedral sites (D1, D2) that differ in values of QS and abundances. As the origin of the difference is not recognizable from Mössbauer measurement, we assume that the Fe^{3+} ions occupy two sites with slightly different symmetry because they have different QS values.

3.5. XPS

Fig. 5 shows the examples of the XPS spectra for the samples $LiMn_{2-x}Ni_xO_4$ and $LiMn_{2-x}Fe_xO_4$ in a wide energy range up to 1400 eV. Besides the lines of elements Li, Mn, Fe, Ni and O forming the compounds, there are extra lines visible from other impurities, coming from the technological process. The C1s lines are especially intense due to the presence of organic technological remains of precursors, as was observed in the literature [62]. The chemical formulas of the measured samples were estimated from the XPS analysis (Table 3 and Table 5). They were used for the calculation of the magnetic moments. Fig. 4 presents deconvolutions of the XPS Mn3p lines into two doublets corresponding to the Mn^{3+} and Mn^{4+} contributions and the Li line. In Table 3 and Table 5, the ratios of Li:Mn and Mn^{3+}:Mn^{4+} are collected.

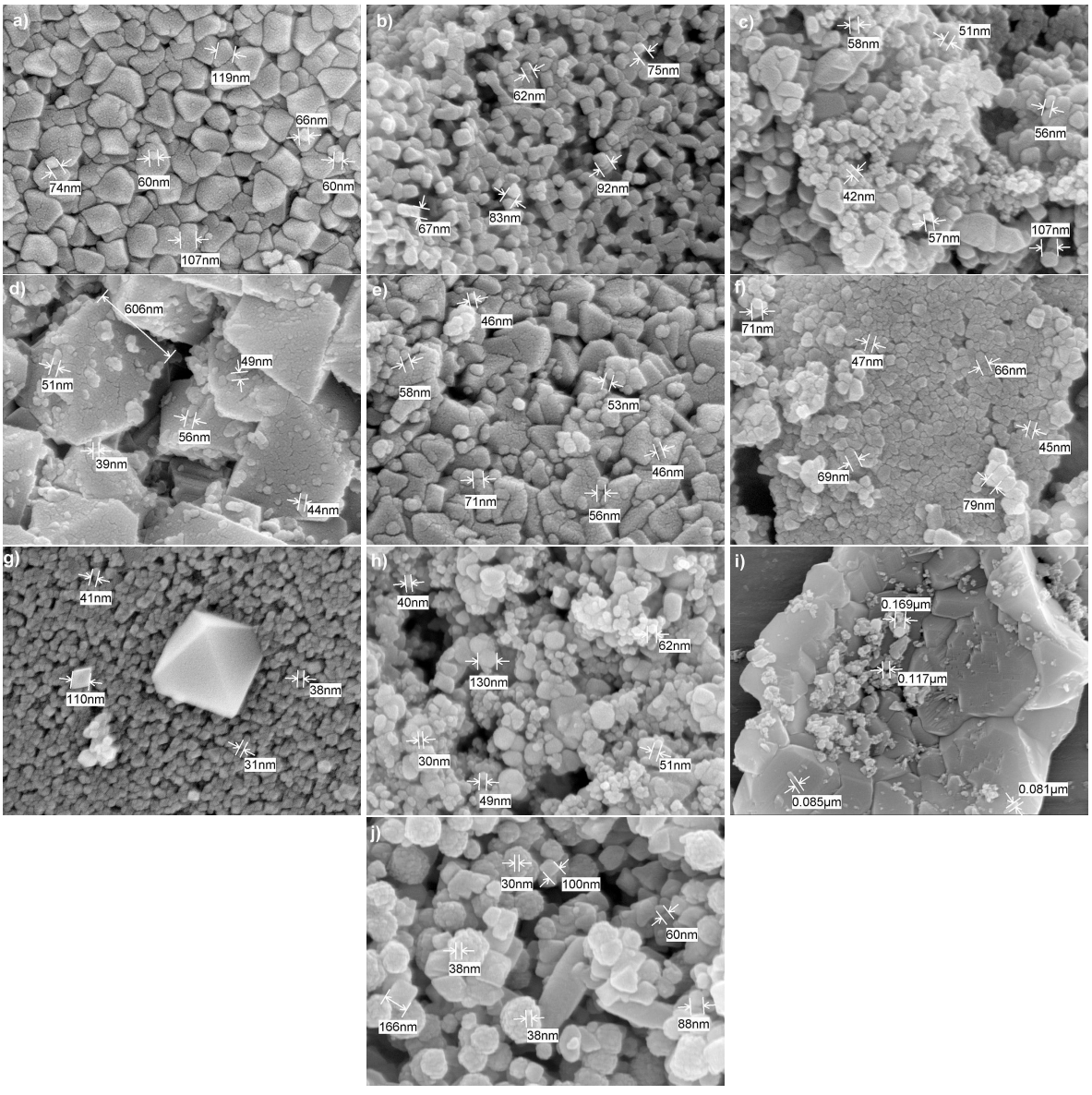

Fig. 3. SEM micrographs of the Ni series: (a) $LiMn_{1.9}Ni_{0.1}O_4$, (b) $LiMn_{1.8}Ni_{0.2}O_4$, (c) $LiMn_{1.7}Ni_{0.3}O_4$, (d) $LiMn_{1.6}Ni_{0.4}O_4$, (e) $LiMn_{1.5}Ni_{0.5}O_4$, and Fe series: (f) $LiMn_{1.9}Fe_{0.1}O_4$, (g) $LiMn_{1.8}Fe_{0.2}O_4$, (h) $LiMn_{1.7}Fe_{0.3}O_4$, (i) $LiMn_{1.6}Fe_{0.4}O_4$, (j) $LiMn_{1.5}Fe_{0.5}O_4$. Magnification 50000×, except (i) where it is 20000×.

Table 3. Chemical compositions and magnetic properties of the Ni series.

XPS composition	Li/(Mn+Ni) 0.5: nominal	PGAA composition	Mn^{3+}/Mn^{4+}	Theta [K]	$\mu_{eff}(\mu_B)$ exp.	$\mu_{eff}(\mu_B)$ calc.
$Li_{1.16}Mn_{1.82}Ni_{0.13}O_{3.89}$	0.60	$LiMn_{1.64}Ni_{0.09}O_y$	0.61	16	6.1	5.9 Mn^{3+}(HS), Mn^{4+}, Ni^{2+}
$Li_{1.36}Mn_{1.93}Ni_{0.27}0_{3.46}$	0.62	$LiMn_{1.44}Ni_{0.16}O_y$	0.59	40	5.9	6.1 Mn^{3+}(HS), Mn^{4+}, Ni^{2+}
*$Li_{1.16}Mn_{1.65}Ni_{0.28}0_{3.92}$	0.60	$LiMn_{1.54}Ni_{0.28}O_y$	0.67	51	4.3	4.6 Mn^{3+}(LS), Mn^{4+}, Ni^{2+}
*$Li_{1.01}Mn_{1.73}Ni_{0.41}O_{3.82}$	0.47	$LiMn_{1.33}Ni_{0.34}O_y$	0.64	110	3.7	5.0 Mn^{3+}(LS), Mn^{4+}, Ni^{2+}
*$Li_{1.17}Mn_{1.59}Ni_{0.67}O_{3.58}$	0.52	$LiMn_{1.29}Ni_{0.44}O_y$	0.95	169	2.5	4.9 Mn^{3+}(LS), Mn^{4+}, Ni^{2+}

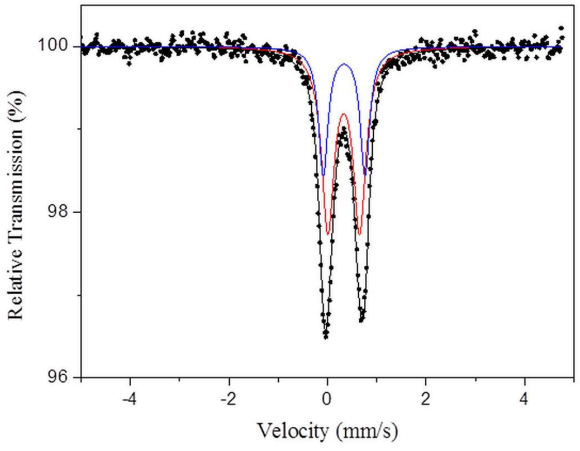

Fig. 4. ^{57}Fe Mössbauer hyperfine parameters of $LiMn_{1.5}Fe_{0.5}O_4$. The fitted subspectra are presented on the spectrum.

Table 4. ^{57}Fe Mössbauer hyperfine parameters of $LiMn_{1.5}Fe_{0.5}O_4$ where A is abundance, IS – isomer shift, QS – quadrupole splitting.

Component	IS [mm/s]	QS [mm/s]	A [%]
D1	0.347±0.003	0.643±0.040	65.17
D2	0.354±0.003	0.846±0.032	34.83

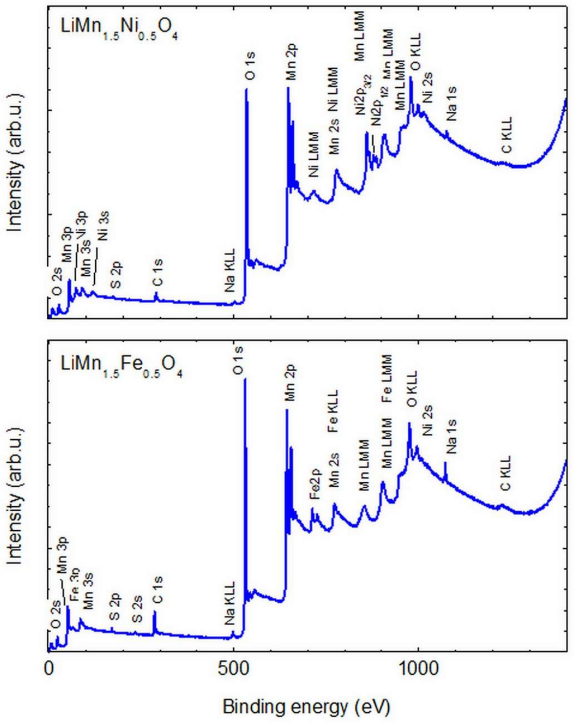

Fig. 5. XPS overview spectra of the samples with x = 0.5 for the Ni and Fe series.

From XRD measurements the decrease of the lattice parameter with increasing Ni amount was observed. The radius of Ni^{2+} (0.69 Å) is larger than that of Mn^{3+}LS (0.58 Å) and similar to Mn^{3+}HS (0.65 Å). Therefore, a transformation of Mn^{3+} into Mn^{4+} (0.53 Å) would explain the decrease of the lattice parameter and the charge balance in the compounds. Such decreased ratios Mn^{3+}/Mn^{4+} are shown in Fig. 6a and Table 3.

For the Fe series, the opposite behavior is observed: the lattice parameters weakly increase with increasing x and Mn^{3+} dominates (Fig. 6b and Table 5). The ionic radii form two groups. The first group contains Fe^{3+} (LS 0.55 Å), Mn^{4+} (0.53 Å), and Mn^{3+} (LS 0.58 Å), whereas Fe^{3+} (HS 0.645 Å) and Mn^{3+} (HS 0.65 Å) make the second one. It is less probable that Fe^{3+} replaces Mn^{4+} due to the charge and radius mismatch. The magnetic measurements indicate that for the samples with x = 0.1 and 0.2, Mn^{3+}LS is substituted by Fe^{3+}LS. For the samples with x = 0.3, Mn^{3+} HS is replaced by Fe^{3+} HS, while for x = 0.4 a mixture of the above states is present. Such separation can explain the nearly constant lattice parameter with increasing x.

The XPS O1s spectra, besides the line (1) related to the compounds (Fig. 7), exhibit some extra lines which can be ascribed to oxygen contamination, defects, etc. Extra lines at lower binding energy are also observed.

The XPS lines of the Fe2p and Ni2p, for the samples with x = 0.5, visible in Fig. 8a and Fig. 8b are related to the Fe^{3+} (in accordance to Mössbauer results) and Ni^{2+} states.

The XPS valence bands exhibit characteristic features of the Mn3d and O2p (Fig. 9). Both valence bands include a mixture of Ni3d or Fe3d states. These results are similar to the results concerning LMO [42, 62] and presented by Wu et al. [65]. The features A and B are related to Mn3d states. The peak A is due to the presence of e_g states of Mn^{3+} HS, while the peak B is attributed

Table 5. Chemical compositions and magnetic properties of the Fe series.

XPS composition	Li/(Mn+Fe) 0.5: nominal	Mn^{3+}/Mn^{4+}	Theta [K] 1 T	$\mu_{eff}(\mu_B)_{exp.}$	$\mu_{eff}(\mu_B)_{calc.}$
$Li_{1.18}Mn_{1.78}Fe_{0.12}O_{3.92}$	0.62	1.54	128	4.88	4.88 $0.75Mn^{3+}$(LS) + $0.25Mn^{3+}$(HS), Mn^{4+}, Fe^{3+}(LS)
$Li_{1.17}Mn_{1.80}Fe_{0.17}O_{3.87}$	0.59	1.17	100	4.86	4.85 $0.82Mn^{3+}$(LS) + $0.18Mn^{3+}$(HS), Mn^{4+}, Fe^{3+}(LS)
$Li_{1.37}Mn_{1.70}Fe_{0.21}O_{3.70}$	0.71	1.09	89	5.65	5.62 $0.4Mn^{3+}$(LS) + $0.6Mn^{3+}$(HS), Mn^{4+}, Fe^{3+}(HS)
$Li_{1.23}Mn_{1.82}Fe_{0.27}O_{3.67}$	0.59	1.33	288	5.20	5.21 $0.8Mn^{3+}$(LS) + $0.2Mn^{3+}$(HS), Mn^{4+}, $2/3Fe^{3+}$(LS) + $1/3Fe^{3+}$(HS)
$Li_{0.91}Mn_{1.66}Fe_{0.31}O_{4.12}$	0.46	1.76	–	–	–

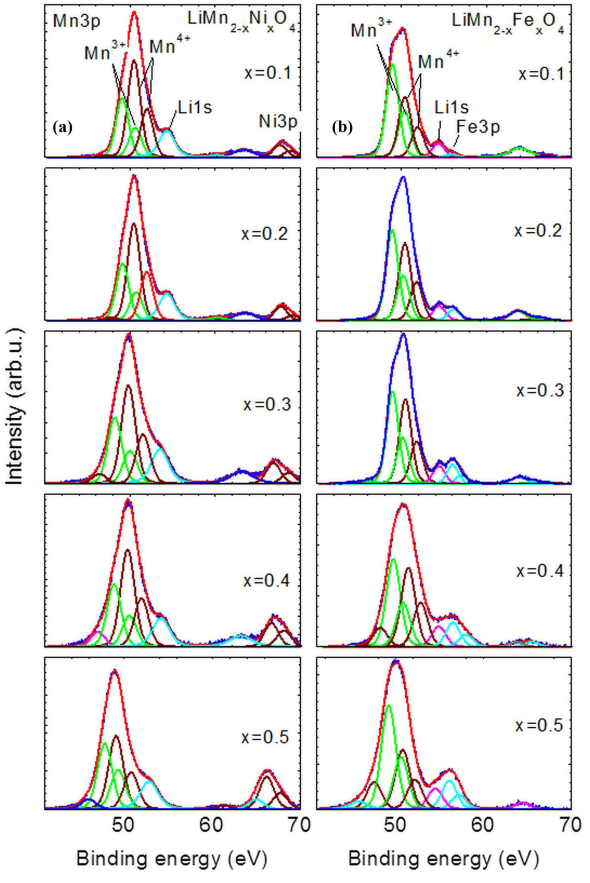

Fig. 6. XPS Mn3p and their deconvolution into synthetic lines of Mn^{3+}, Mn^{4+} and Li1s for (a) the Ni series and (b) the Fe series.

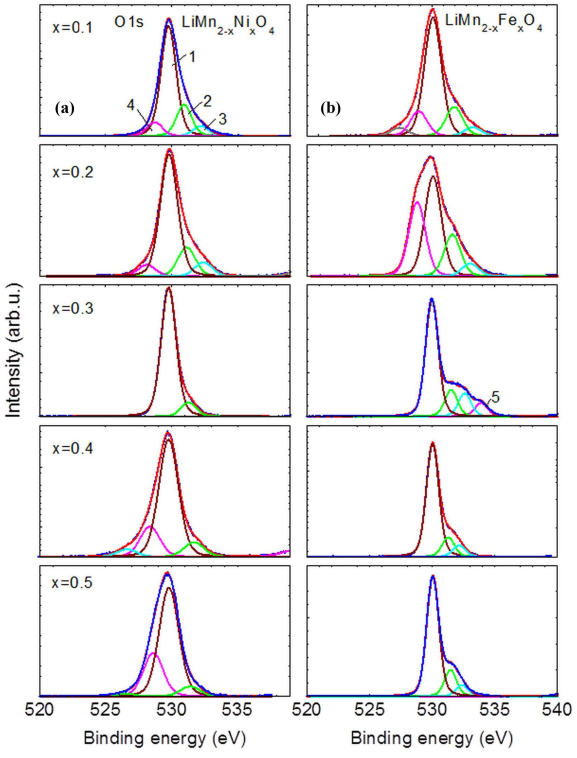

Fig. 7. XPS O1s of (a) the Ni and (b) Fe series. 1 marks oxygen in the compound, 2 to 5 enumerate additional lines.

to the t_{2g} states of Mn^{3+} and Mn^{4+}. The features C and D are ascribed to O2p. The features E and F may be due to some oxide contamination.

3.6. Magnetic measurements

Measurements of the magnetic susceptibility χ showed magnetic irreversibility, zero-field-cooled and field-cooled for the samples containing Ni and Fe. Fig. 10 shows several examples of magnetic susceptibility runs. No signature of Jahn-Teller transition was observed in the substituted compounds measured in this work.

The applied magnetic field was 1 T. The Ni substituted samples start ordering below 150 K. The magnetic susceptibility measurements of the majority of the samples can be better fit according to the relation using the Neél theory:

$$\frac{1}{\chi} = \frac{1}{\chi_0} + \frac{T}{C} - \frac{\sigma}{T-\theta} \qquad (1)$$

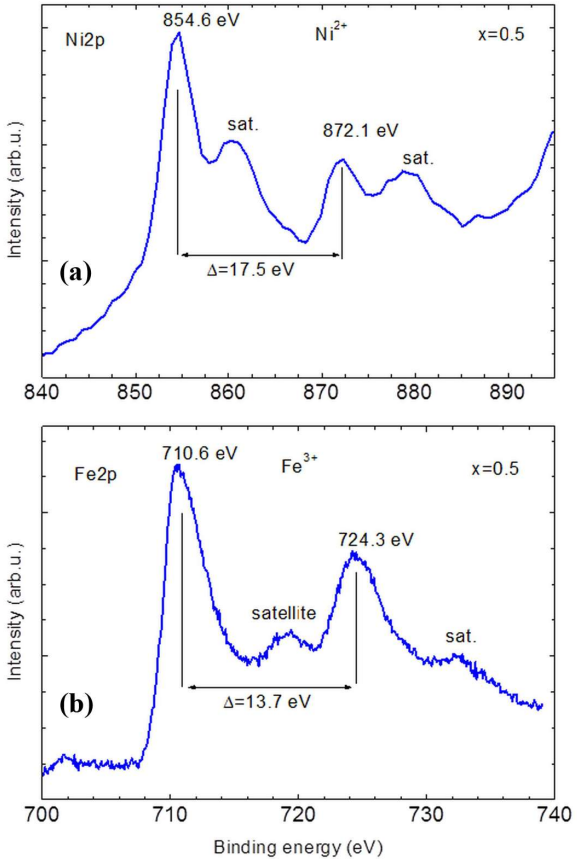

Fig. 8. XPS of the Ni2p (a) and Fe2p (b) lines.

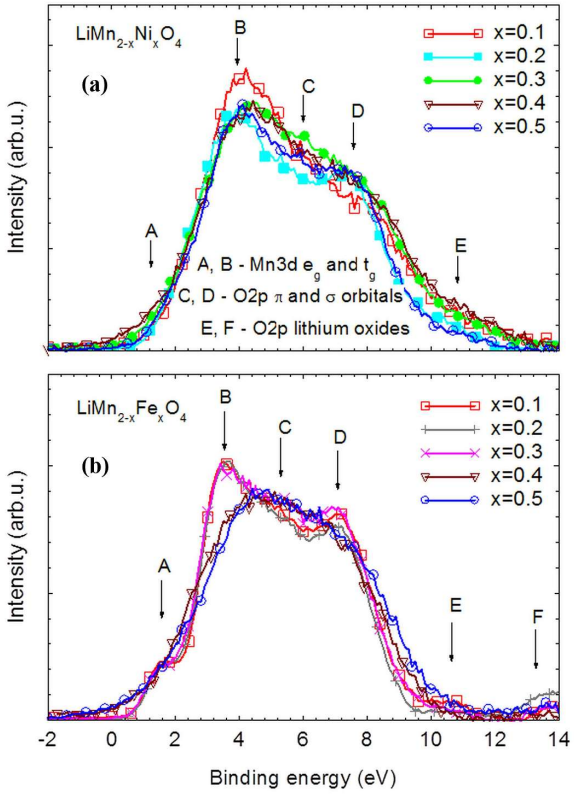

Fig. 9. The XPS spectrum of valence bands.

where C is the Curie constant, θ is the paramagnetic Curie temperature, χ_0 and σ are parameters evaluated from the fit, and T is the temperature in Kelvin. This indicates uncompensated antiferromagnetic character. For the samples with x = 0.4 and 0.5 the inverse of the susceptibility was fitted according to the Curie-Weiss law:

$$\frac{1}{\chi} = \frac{1}{\chi_0 + \frac{C}{T-\theta}} \qquad (2)$$

The effective magnetic moment depends on the amount of manganese and the ratio Mn^{3+}:Mn^{4+} and Ni^{2+} amount (Table 3). $Mn(3d^4)^{3+}$ with HS (high spin) has a magnetic moment of 4.90 μ_B, while $Mn(3d^4)^{3+}$ with LS (low spin) and $Mn(3d^3)^{4+}$ have magnetic moments of 2.83 μ_B and 3.87 μ_B, respectively. According to the XPS results, the Ni magnetic contribution is $Ni(3d^8)^{2+}$ equal to 2.83 μ_B.

For the samples doped with Fe, measurements at magnetic field of 1 T allow fitting the curves for x = 0.1 – 0.4 using the Neél theory (Fig. 10). The calculations of the effective magnetic moments for the mixture of Mn^{3+} LS and HS and Fe^{3+} LS (1.75 μ_B) and HS (5.92 μ_B), gave good agreement with experimental values (Table 5).

The XPS valence band characters for the Ni and Fe substituted samples reflect magnetic states of the samples (Fig. 9). For the samples containing Fe for x from 0.1 to 0.3 the features A, B, C and D (described in Fig. 9b) are well separated. These samples measured at room temperature are in the paramagnetic state. The samples with x = 0.4 and 0.5 are in ordered state. They have the highest admixture of Fe3d states in the valence band. However, the features A to D are difficult to distinguish. Both above mentioned reasons can be responsible for the change of the shape of the valence band states.

For Ni containing samples, the shapes of the valence bands are similar, blurred (not visible

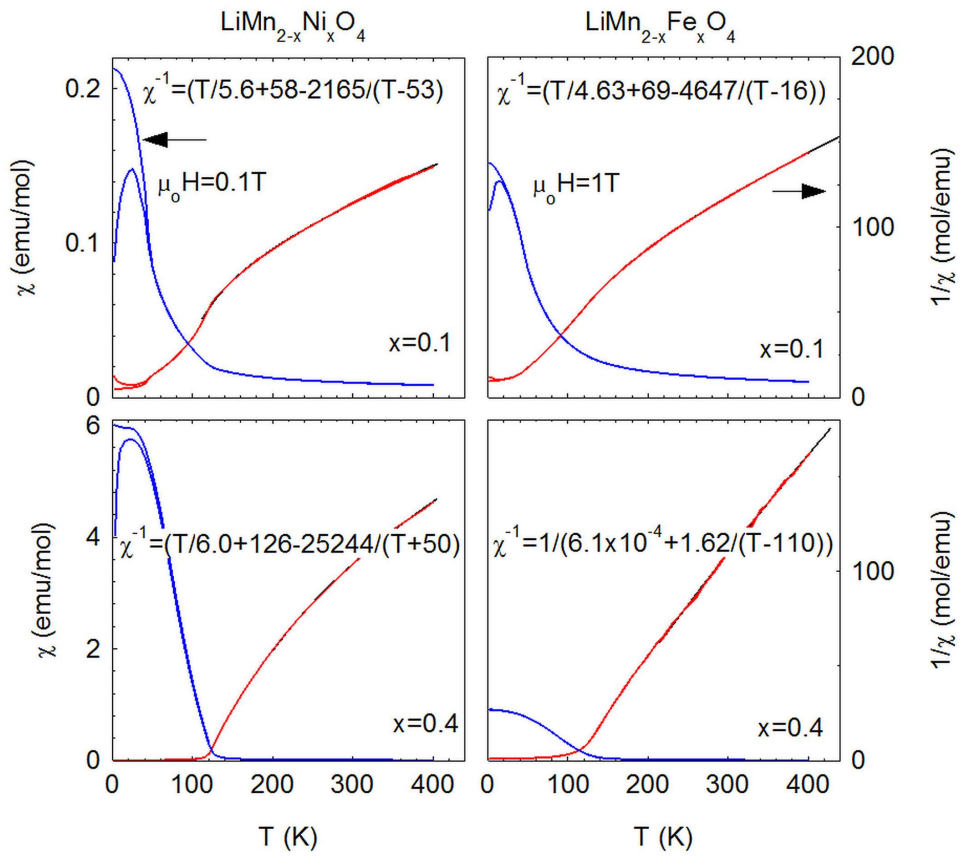

Fig. 10. Magnetic susceptibility of (a) the Ni series and (b) the Fe series measured under 1 T.

Table 6. Structural parameters for the $LiMn_{2-x}Ni_xO_4$ series.

x	Anion parameter	Size K_{00}	Size K_{41}	Strain S_{400}	Strain S_{220}	ADP [Å^2]		
						Li	Mn/Ni	O
0.1	0.2697(3)	1.10(2)	–	0.62(2)	–	3.3(7)	3.87(7)	3.7(1)
0.2	0.2686(4)	3.00(9)	1.3(2)	0.22(5)	1.0(2)	12(1)	3.67(9)	3.3(1)
0.3	0.2587(3)	2.56(7)	2.6(2)	0.36(6)	3.3(2)	3.0(fix)	2.04(6)	2.8(1)
0.4	0.2594(3)	1.60(7)	1.8(1)	0.98(7)	4.7(2)	3.0(fix)	1.70(5)	2.7(1)
0.5	0.2710(3)	2.34(4)	–	0.15(2)	–	9.0(1.0)	4.4(1)	3.3(2)

Table 7. Structural parameters for the $LiMn_{2-x}Fe_xO_4$ series.

x	Anion parameter	Size K_{00}	Size K_{41}	Strain S_{400}	Strain S_{220}	ADP [Å^2]		
						Li	Mn/Fe	O
0.1	0.2704(3)	1.55(2)	–	0.23(1)	–	6.3(9)	4.68(8)	5.5(2)
0.2	0.2695(3)	2.3(3)	–	0.19(2)	–	2.8(7)	3.82(8)	4.7(2)
0.3	0.2697(3)	2.00(3)	–	0.25(2)	–	3.7(8)	4.2(1)	5.1(1)
0.4	0.2663(2)	0.40(1)	–	0.48(1)	–	1.0(4)	3.22(5)	4.2(1)
0.5	0.2646(2)	0.88(2)	–	0.60(1)	–	–0.1(3)	2.66(5)	3.8(1)

$Mn3de_g$ states (feature A). This may reflect not only the paramagnetic state but the admixture of the second phase, as well.

There are some theoretical papers claiming that existence of Mn^{3+} LS is possible under high pressure for cubic spinel structure [66]. However, in case of the examined samples the primitive cell volumes for $LiMn_2O_4$ (138.2 Å^3) and $LiMn_{1.5}Ni_{0.5}O_4$ (136.2 Å^3) are located in the region where the energies of the Mn^{3+} LS and HS are comparable.

4. Conclusions

The Jahn-Teller distortion was eliminated in the examined samples. The XPS Fe2p and Ni2p lines confirmed the ionic states of Fe^{3+} and Ni^{2+}. The Mössbauer spectroscopy restricted the Fe^{3+} ion positions only to the octahedral sites. The valence bands measured in ordered and paramagnetic states differed due to broadening caused by the molecular magnetic field. The Mn^{3+} ions dominated in the iron substituted series, whereas Mn^{4+} dominated in the nickel one. The Pechini sol-gel method did not fully control the dopant concentration within the substitution range.

Acknowledgements

SQUID magnetometer was financed by the European Regional Development Fund, whereas SEM/EDS JEOL was financed by the Regional Fund for Environmental Protection in Katowice.

References

[1] MARZEC J., ŚWIERCZEK K., PRZEWOŹNIK J., MOLENDA J., SIMON D.R., KELDER E.M., SCHOONMAN J., *Solid State Ionics*, 146 (2002), 225.
[2] KITAMURA N., IWATSUKI H., IDEMOTO Y.J., *J. Power Sources*, 189 (2009), 114.
[3] WANG X., CHEN X., GAO L., ZHENG H., JI M., SHEN T., ZHANG Z., *J. Cryst. Growth*, 256 (2003), 123.
[4] HE X., WANG L., PU W., ZHANG G., JIANG C., WAN C., *Int. J. Electrochem. Sc.*, 1 (2006), 12.
[5] MICHALSKA M., LIPIŃSKA L., MIRKOWSKA M., AKSIENIONEK M., DIDUSZKO R., WASIUCIONEK M., *Solid State Ionics*, 188 (2011), 160.
[6] MICHALSKA M., LIPIŃSKA L., DIDUSZKO R., MAZURKIEWICZ M., MAŁOLEPSZY A., STOBINSKI L., KURZYDŁOWSKI K.J., *Phys. Status Solidi C*, 8 (2011), 2538.
[7] FU Y.-P., SU Y.-H., LIN C.-H., WU S.-H., *Ceram. Int.*, 35 (2009), 3463.
[8] WHITTINGHAM M.S., *Chem. Rev.*, 104 (2004), 4271.
[9] JULIEN C.M., *Mater. Sci. Eng.*, R 40 (2003), 47.
[10] WAN C., WU M., WU D., *Powder Technol.*, 199 (2010), 154.
[11] SCROSATI B., GARCHE J., *J. Power Sources*, 195 (2010), 2419.
[12] THACKERAY M.M., *Prog. Solid State Ch.*, 25 (1997), 1.
[13] FERGUS J.W., *J. Power Sources*, 195 (2010), 939.
[14] SINGH P., SIL A., NATH M., RAY S., *Physica B*, 405 (2010), 649–654.
[15] SURYAKALA K., PARUTHIMAL KALAIGNAN G., VASUDEVAN T., *Int. J. Electrochem. Sc.*, 1 (2006), 372.
[16] THIRUNAKARAN R., SIVASHANMUGAM A., GOPUKUMAR S., DUNNILL C.W., GREGORY D.H., *J. Mater. Process. Tech.*, 208 (2008), 520.
[17] THIRUNAKARAN R., SIVASHANMUGAM A., GOPUKUMAR S., DUNNILL C.W., GREGORY D.H., *J. Phys. Chem. Solids*, 69 (2008), 2082.
[18] SHAO-HORN Y., MIDDAUGH R.L., *Solid State Ionics*, 139 (2001), 13.
[19] YI T., HU X., GAO K., *J. Power Sources*, 162 (2006), 636.
[20] YI T.-F., ZHU Y.-R., ZHU R.-S., *Solid State Ionics*, 179 (2008), 2132.
[21] BERG H., THOMAS J.O., LIU W., FARRINGTON G.C., *Solid State Ionics*, 112 (1998), 165.
[22] CHEN Z., QIU S., CAO Y., AI X., XIE K., HONG X., YANG H., *J. Mater. Chem.*, 22 (2012), 17768.
[23] DONG Y., WANG Z., QIN H., SUI X., *RSC Adv.*, 2 (2012), 11988.
[24] WANG F.X., XIAO S.Y., SHI Y., LIU L.L., ZHU Y.S., WU Y.P., WANG J.Z., HOLZE R., *Electrochim. Acta*, 93 (2013), 301.
[25] XU Y., CHEN G., FU E., ZHOU M., DUNWELL M., FEI L., DENG S., ANDERSEN P., WANG Y., JIA Q., LUO H., *RSC Adv.*, 3 (2013), 18441.
[26] HAI B., SHUKLA A.K., DUNCAN H., CHEN G., *J. Mater. Chem. A*, 1 (2013), 759.
[27] WEI Q., WANG X., YANG X., JU B., HU B., SHU H., WEN W., ZHOU M., SONG Y., WU H., HU H., *J. Mater. Chem. A*, 1 (2013), 4010.
[28] CHEN Z., ZHAO R., DU P., HU H., WANG T., ZHU L., CHEN H., *J. Mater. Chem. A*, 2 (2014), 12835.
[29] MANTHIRAM A., CHEMELEWSKI K., LEE E.-S., *Energy Environ. Sci.*, 7 (2014), 1339.
[30] WANG J., YU Y., WU B., LIN W., LI J., ZHAO J., *J. Mater. Chem. A*, 3 (2015), 2353.
[31] WU Q., YIN Y., SUN S., ZHANG X., WAN N., BAI Y., *Electrochim. Acta*, 158 (2015), 73.
[32] SONG M., AHN D., *Solid State Ionics*, 112 (1998), 245.
[33] TSUJI T., NAGAO M., YAMAMURA Y., TAI N.T., *Solid State Ionics*, 154–155 (2002), 381.
[34] MALYOVANYI S.M., ANDRIIKO A.A., MONKO A.P., *J. Solid State Electr.*, 8 (2003), 7.
[35] KIM B.-H., CHOI Y.-K., CHOA Y.-H., *Solid State Ionics*, 158 (2003), 281.

[36] TANIGUCHI I., BAKENOV Z., *Powder Technol.*, 159 (2005), 55.
[37] WOLSKA E., PISZORA P., STEMPIN K., CATLOW C.R.A., *J. Alloy. Compd.*, 286 (1999), 203.
[38] WOLSKA E., TOVAR M., ANDRZEJEWSKI B., NOWICKI W., DARUL J., PISZORA P., KNAPP M., *Solid State Sci.*, 8 (2006), 31.
[39] MATEYSHINA YU G., LAFONT U., UVAROV N.F., KELDER E.M., *Solid State Ionics*, 179 (2008), 192.
[40] PICO M.P., ALVAREZ-SERRANO L., LOPEZ M.L., VEIGA M.L., *Dalton Trans.*, 43 (2014), 14787.
[41] SHI Y., ZHU S., ZHU C., LI Y., CHEN Z., ZHANG D., *Electrochim. Acta*, 154 (2015), 17.
[42] TALIK E., LIPIŃSKA L., ZAJDEL P., ZAŁÓG A., MICHALSKA M., GUZIK A., *J. Solid State Chem.*, 206 (2013), 257.
[43] MICHALSKA M., HAMANKIEWICZ B., ZIÓŁKOWSKA D., KRAJEWSKI M., LIPIŃSKA L., ANDRZEJCZUK M., CZERWIŃSKI A., *Electrochim. Acta*, 136 (2014), 286.
[44] HAMANKIEWICZ B., MICHALSKA M., KRAJEWSKI M., ZIÓŁKOWSKA D., LIPIŃSKA L., KAMIŃSKA M., CZERWIŃSKI A., *Solid State Ionics*, 262 (2014), 9.
[45] MICHALSKA M., LIPIŃSKA L., SIKORA A., ZIÓŁKOWSKA D., KORONA K.P., ANDRZEJCZUK M., *J. Alloy. Compd.*, 632 (2015), 256.
[46] RIETVELD H.M., *J. Appl. Crystallogr.*, 2 (1969), 65.
[47] RODRIGUEZ-CARVAJAL J., *Commission on Powder Diffraction Newsletters*, 26 (2011), 12-19.
[48] THOMPSON P., COX D.E., HASTINGS J.B., *J. Appl. Crystallogr.*, 20 (1987), 20.
[49] STEPHENS P.W., *J. Appl. Crystallogr.*, 32 (1999), 281.
[50] JARVINEN M., *J. Appl. Crystallogr.*, 26 (1993), 527.
[51] BELLITTO C., BAUER E.M., RIGHINI G., GREEN M.A., BRANFORD W.R., ANTONINI A., PASQUALI M., *J. Phys. Chem. Solids*, 65 (2004), 29.
[52] BRANFORD W., GREEN M.A., NEUMANN D.A., *Chem. Mater.*, 14 (2002), 1649.
[53] BRIK M.G., AVRAM N.M., AVRAM C.N., RUDOWICZ C., YEUNG Y.Y., GNUTEK P., *J. Alloy. Compd.*, 432 (2007), 61.
[54] ZAJDEL P., JENDRZEJEWSKA I., GORAUS J., DUDA H., GORYCZKA T., KITA A., *Radiat. Phys. Chem.*, 80(10) (2011), 1008.
[55] YOON W.-S., BALASUBRAMANIAN M., YANG X.-Q., FU Z., FISCHER D.A., MCBREENA J., *J. Electrochem. Soc.*, 151(2) (2004), A246.
[56] *Multipak Software Version 6*, Physical Electronics, Minnesota, 1998.
[57] PAUL R.L., LINDSTROM R.M., HEALD A.E., *J. Radioanal. Nucl. Ch.*, 215(1) (1997), 63.
[58] PAUL R.L., LINDSTROM R.M., *J. Radioanal. Nucl. Ch.*, 243 (2000), 181.
[59] PAUL R.L., *Am. Lab.*, 34(3) (2002), 15.
[60] LINDSTROM R.M., *Biol. Trace Elem. Res.*, 43-45 (1994), 597.
[61] RODRIGUEZ-CARVAJAL J., ROUSSE G., MASQUELIER C., HERVIEU M., *Phys. Rev. Lett.*, 81 (21) (1998), 4660.
[62] TALIK E., ZAŁÓG A., SKRZYPEK D., GUZIK A., ZAJDEL P., MICHALSKA M., LIPIŃSKA L., *Cryst. Res. Technol.*, 47 (3) (2012), 351.
[63] SHANNON R.D., *Acta Crystallogr. A*, 32 (1976), 751.
[64] STROBEL P., CRAS LE F., SEGUIN L., ANNE M., TARASCON J.M., *J. Solid State Chem.*, 135 (1998), 132.
[65] WU Q.H., THISSEN A., JAEGERMANN W., *Chinese Phys. Lett.*, 23 (2006), 2202.
[66] VEN VAN DER A., MARIANETTI C., MORGAN D., CEDER G., *Solid State Ionics*, 135 (2000), 21.

Received 2016-02-08
Accepted 2016-12-12